Am J Transl Res 2025;17(8):6347-6358
www.ajtr.org /ISSN:1943-8141/AJTR0164465

Original Article

Antimicrobial drug-derived carbon quantum dots for photodynamic therapy of bedsores and bacterial infections

Qianwen Bi[1], Fumin Zheng[2], Ziqin Lu[1], Jia Sun[1]

[1]Department of Rehabilitation Medicine, Zhejiang Hospital, No. 12 Lingyin Road, Hangzhou 310000, Zhejiang, P. R. China; [2]School of Stomatology, Qingdao University, No. 380 Ningxia Road, Qingdao 266000, Shandong, P. R. China

Received March 11, 2025; Accepted July 5, 2025; Epub August 15, 2025; Published August 30, 2025

Abstract: Objectives: Bedsores (pressure ulcers) exhibit high incidence rates (0.4-38%) and prolonged recovery periods, with bacterial infections posing the most frequent and severe complications, significantly impeding wound healing. Conventional antibiotic therapies face limitations due to antimicrobial resistance, necessitating innovative strategies with enhanced biocompatibility and reduced resistance-inducing potential. This study aimed to develop a photodynamic therapy (PDT)-based antimicrobial approach by converting antimicrobial drugs into N-doped carbon quantum dots (N, CQ-dots) for efficient bacterial inhibition in wound environments. Methods: N, CQ-dots were synthesized from protocatechuic acid (a natural antimicrobial metabolite) via solvothermal method, preserving critical functional groups (-COOH, -OH) inherited from the precursor. Structural and optical properties were characterized using transmission electron microscopy (TEM), X-ray photoelectron spectroscopy (XPS), and ultraviolet-to-visible (UV-Vis) spectroscopy. Photodynamic antimicrobial efficacy was evaluated against Staphylococcus aureus and Escherichia coli through colony-count assays, and live/dead staining. Results: The synthesized N, CQ-dots exhibited uniform morphology (~3.5 nm) and abundant oxygen-containing functional groups, as confirmed by XPS and Fourier Transform Infrared (FTIR) spectrometer analysis. Under irradiation, the material demonstrated potent antibacterial activity, achieving >99.9% viability reduction in Gram-positive and Gram-negative strains, with minimal cytotoxicity (MBC >100 μg/mL). Conclusions: This work demonstrates a novel paradigm for transforming antimicrobial drugs into multifunctional N, CQ-dots, leveraging preserved pharmacophores and PDT mechanisms to overcome drug resistance. The system combines intrinsic antibacterial activity with light-triggered responsiveness, offering a promising solution for managing infected bedsores while minimizing systemic toxicity. These findings highlight the translational potential of drug-derived nanomaterials in precision wound care.

Keywords: Bedsores, antibacterial, carbon quantum dots, photodynamic therapy, solvothermal method

Introduction

Prolonged immobilization during recovery phases, such as in bedridden or paraplegic patients, predisposes cutaneous tissues to sustained pressure-induced ischemia, culminating in pressure ulcer development [1, 2]. Characterized by epidemic prevalence (up to 38% incidence), refractory healing dynamics, and recurrent episodes [3, 4], these lesions predominantly affect geriatric populations [5]. Metabolic impairments, including malnutrition, diabetes mellitus, and venous insufficiency, further compromise wound resolution [6], escalating risks of osteomyelitic infections, septicemia, and hypoproteinemia [7]. Such complications exacerbate clinical management complexities, with mortality rates reaching 25% in severe cases [8]. Despite advances in wound care, bacterial colonization remains a principal impediment to tissue regeneration [9]. Current therapeutic paradigms primarily rely on topical antimicrobial agents for superficial infections [10], escalating to systemic antibiotic administration when microbial invasion penetrates deeper tissue strata [11]. Deep tissue infections require systemic antibiotics, with initial intravenous therapy transitioning to oral regimens upon clinical improvement, while severe cases may escalate to optimized parenteral strategies [12]. However, excessive antimicrobial utilization correlates with dysbiosis, hepa-

https://doi.org/10.62347/YELM3779

torenal dysfunction and the emergence of multidrug-resistant pathogens, underscoring urgent demands for innovative biocompatible antimicrobial strategies.

Photodynamic therapy (PDT) is a minimally invasive modality that employs photochemical or photophysical mechanisms to eradicate pathogens through the conversion of light energy into reactive oxygen species (ROS) or localized thermal energy [13]. Central to PDT advancement is the engineering of nanomaterials exhibiting exceptional photon-to-ROS conversion efficiency, including noble metal-based constructs, semiconductor systems, organic photosensitizers, carbon nanomaterials, *etc* [14]. However, these materials often exhibit prohibitive costs, cytotoxic profiles, and suboptimal photostability, thereby constraining their clinical translation. Consequently, there remains a critical demand for developing multifunctional materials that synergize robust PDT efficacy, economic feasibility, biosafety, and scalable synthesis to overcome antimicrobial resistance challenges in pressure ulcer management while enhancing bacterial eradication outcomes. Carbon quantum dots (CQ-dots), a class of carbon-based nanomaterials primarily constituted by carbon, hydrogen, oxygen, and nitrogen elements, demonstrate multidisciplinary applications in antimicrobial therapy, oncotherapy, and bioimaging owing to their exceptional biocompatibility, low cytotoxicity, precursor abundance, and photostability [12, 15, 16]. Protocatechuic acid, a pleiotropic polyphenol metabolite exhibiting antibacterial, antioxidant, anti-inflammatory, antihyperglycemic and neuroprotective activities, is ubiquitously distributed in botanical species and fruits. This compound undergoes efficient bioavailability in mammalian systems through gastrointestinal absorption [17-19].

To circumvent antimicrobial resistance challenges, this study engineered nitrogen-doped carbon quantum dots (N, CQ-dots) through a solvothermal protocol utilizing protocatechuic acid as the exclusive carbon precursor. Structural characterization via nuclear magnetic resonance (NMR) and Fourier-transform infrared spectroscopy (FTIR) revealed preserved pharmacophoric motifs (-COOH, -OH) inherited from the precursor. In vitro antimicrobial assays demonstrated exceptional bactericidal efficacy, achieving >99.9% viability reduction against multidrug-resistant pathogens. This pioneering strategy transforms natural antimicrobial metabolites into functional nanomaterials, synergistically enhancing photodynamic inactivation capabilities. The developed N, CQ-dots offer a biocompatible, scalable platform for combating recalcitrant infections in pressure ulcer management.

Materials and methods

Materials

Protocatechuic acid (≥97%) and N, N-Dimethylformamide (DMF, ≥99.9%) were purchased from Aladin (Shanghai Aladdin Biochemical Technology Co., Ltd., Shanghai, China). Dichloromethane (≥99.9%) and methanol (≥99.9%) were purchased from Thain Chemical Technology Co., Ltd., (Shanghai, China). SYTO 9/PI live/dead bacterial double stain kit and phosphate buffer saline (PBS) were provided by Beijing Solaibao Technology Co., Ltd. China. Sangon Biotech (Shanghai, China) was responsible for supplying Luria-Bertani (LB) broth and LB broth agar.

Synthesis of the N, CQ-dots

As shown in **Scheme 1**, N, CQ-dots were synthesized via solvothermal method with protocatechuic as precursor, DMF as solvent, and H_2SO_4 as the catalyst. Firstly, 0.25 g of protocatechuic and 1 mL H_2SO_4 (33%) were dissolved in 60 mL of DMF to form a homogeneous solution. Subsequent sonication for 10 minutes yielded a transparent solution, which was transferred to a 100 mL stainless-steel autoclave lined with polytetrafluoroethylene (PTFE) and heated at 180°C for 12 h. Then, the reactors were cooled to ambient temperature naturally. The resultant solution was concentrated and subjected to purification through silica gel column chromatography (300-500 mesh) using a dichloromethane/methanol gradient (10:1) as the eluent. Subsequently, the byproducts were dialyzed for 8 h through a 1,000 Da dialysis membrane with deionized water to remove byproducts. Finally, the purified N, CQ-dots powder were obtained by freeze-drying.

Bacterial cell culture

The antibacterial efficacy of N, CQ-dots was evaluated against *Escherichia coli* (*E. coli*, ATCC

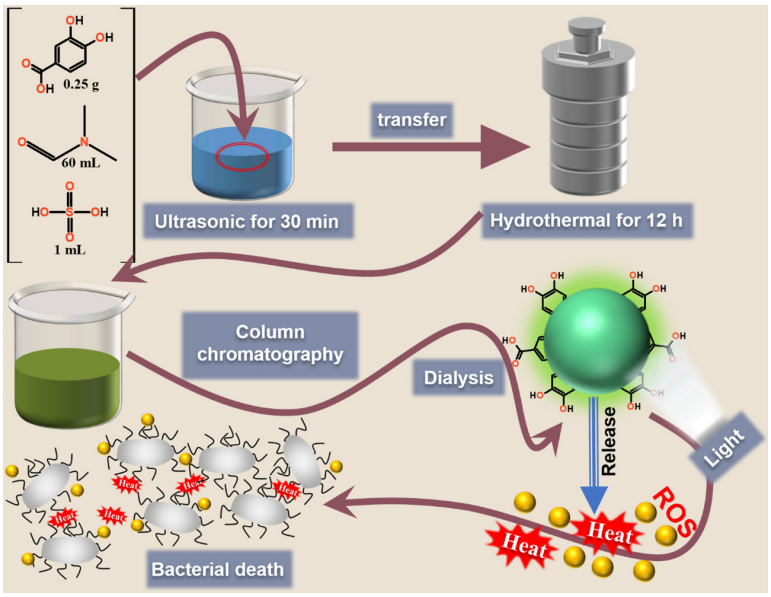

Scheme 1. Schematic illustration of the preparation and antibacterial application of the N-doped carbon quantum dots (N, CQ-dots).

9637) and *Staphylococcus aureus* (*S. aureus*, ATCC 25923). Initially, the standardized bacterial suspension was cultured at 37°C for 24 h. After that, 5 mL of Luria-Bertani (LB) broth culture medium was incubated with 500 μL of bacteria suspension (either *E. coli* or *S. aureus*, 5 × 10^9 CFU/mL). In a shaking incubator at 150 rpm, the medium was cultured overnight at 37°C. Subsequent photodynamic treatment protocols were made by diluting the bacteria to 1 × 10^6 CFU/mL.

Antibacterial performance

For experimental evaluation, 100 μg of N, CQ-dots were suspended into 1 mL of bacterial suspension and designed as the experimental group, while 100 μL of the phosphate-buffered saline (PBS) supplemented with identical bacterial volume served as the control group. Following a 6 h co-cultivation period at 37°C, samples underwent 808 nm laser irradiation (0.3 W/cm^2) for different times and cultured for 18 h. Subsequently, 10 μL aliquots were uniformly plated onto agar media and incubated overnight at 37°C to facilitate colony formation. Quantitative analysis of antimicrobial efficacy was performed through colony enumeration and photographic documentation, with statistical validation against baseline controls.

Bacterial live/dead staining

Bacterial suspensions (10^4 CFU/mL) were exposed to either PBS or N, CQ-dots (100 μg/mL) for 6 h, followed by 5 min of 808 nm laser irradiation (0.3 W/cm^2). Subsequent post-incubation for 18 hours at 37°C was conducted to assess delayed cytotoxic effects. Staining was performed using the LIVE/DEAD™ BacLight™ Bacterial Viability Kit, where samples were incubated for 15 minutes at room temperature in darkness, then rinsed thrice with PBS to remove unbound dye. Following this, the stained bacterial suspension (5 μL) was placed on a slide and the fluorescence image was imaged using a confocal microscope.

Bacterial morphology observation

The bacterial suspensions (10^4 CFU/mL) were exposed to PBS or N, CQ-dots (100 μg/mL) for 6 h, subjected to 808 nm laser irradiation (0.3 W/cm^2) for 5 min. Subsequent post-irradiation incubation was conducted for 18 h at 37°C to assess delayed cytotoxic effects. Afterwards, cells were collected by centrifugation, and placed in 2.5% glutaraldehyde for 2 h at room temperature. Dehydration followed, using an ethanol dilution series of increasing concentrations (10-100%) for 15 min. Final samples were sputter-coated with gold and examined via (scanning electron microscope) SEM for morphological analysis.

Statistical analysis

All experiments were performed in triplicate (n=3 biological replicates), with triplicate technical replicates per sample, following standardized protocols for reproducibility assessment. Comparative analyses utilized Student's t-test (two-tailed) for pairwise comparisons or one-way ANOVA with Dunnett's post-hoc correction for multiple group comparisons. Significance thresholds were set at *P<0.05 (*), P<0.01 (**),*

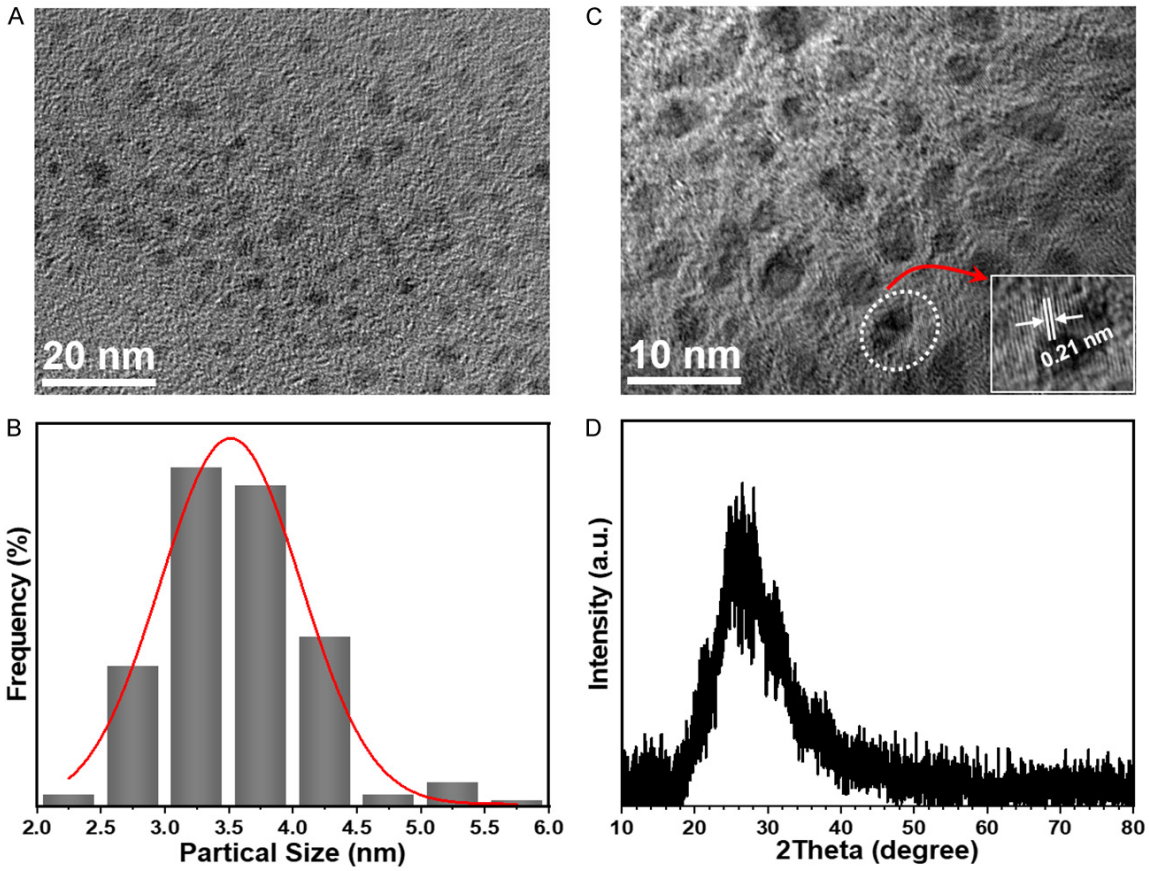

Figure 1. Morphology, and structure properties of the N, CQ-dots. A. Transmission electron microscope (TEM) image of the N, CQ-dots. B. Particle size distribution histogram of the N, CQ-dots. C. High-resolution TEM image of the N, CQ-dots. D. X-ray diffraction (XRD) pattern of the N, CQ-dots.

and P<0.001 (***), as established in quantitative biological studies.

Characterization

Applied transmission electron microscope (TEM, JEM-2100F, Japan) and X-ray diffraction with Cu Kα radiation (Rigaku Smartab, 3KW) to character the morphology and components of N, CQ-dots. Fluorescence spectrophotometer (F-2700 Hitachi, Japan), ultraviolet-visible (UV-Vis) absorption spectrophotometer (Avaspec-2048-2-USB2, Avantes, Netherland), fourier transform infrared spectrometer (FTIR, Nicolet 6700, Thermo Scientific, USA), and Superconducting Nuclear Magnetic Resonance spectroscopy (NMR, 600 MHz, Avance III, Germany) were employed to record the vibrations of optical spectra. The morphological bacterial changes were monitored by scanning electron microscopy (SEM, Hitachi, Tokyo, Japan). Fluorescence images were acquired by confocal laser scanning microscope (CLSM, Leica TCS SP8 STED 3X). 808 nm diode laser was produced from JPT Opto-electronics Co., Ltd. (Shenzhen, China).

Results

Structure analysis

As shown in **Figure 1A**, transmission electron microscope (TEM) analysis at 20 nm resolution demonstrates the uniform dispersion of synthesized N, CQ-dots with minimal agglomeration, exhibiting an average diameter of 3.5 nm (**Figure 1B**). High-resolution TEM (HR-TEM) image (**Figure 1C**) indicates an interplanar spacing of 0.21 nm, corresponding to the (100) lattice plane of graphitic carbon [20]. Furthermore, the X-ray diffraction (XRD) pattern (**Figure 1D**) displays a broad diffraction peak centered at 25.5°, which aligns with the (002) crystallographic plane of graphite - a hallmark

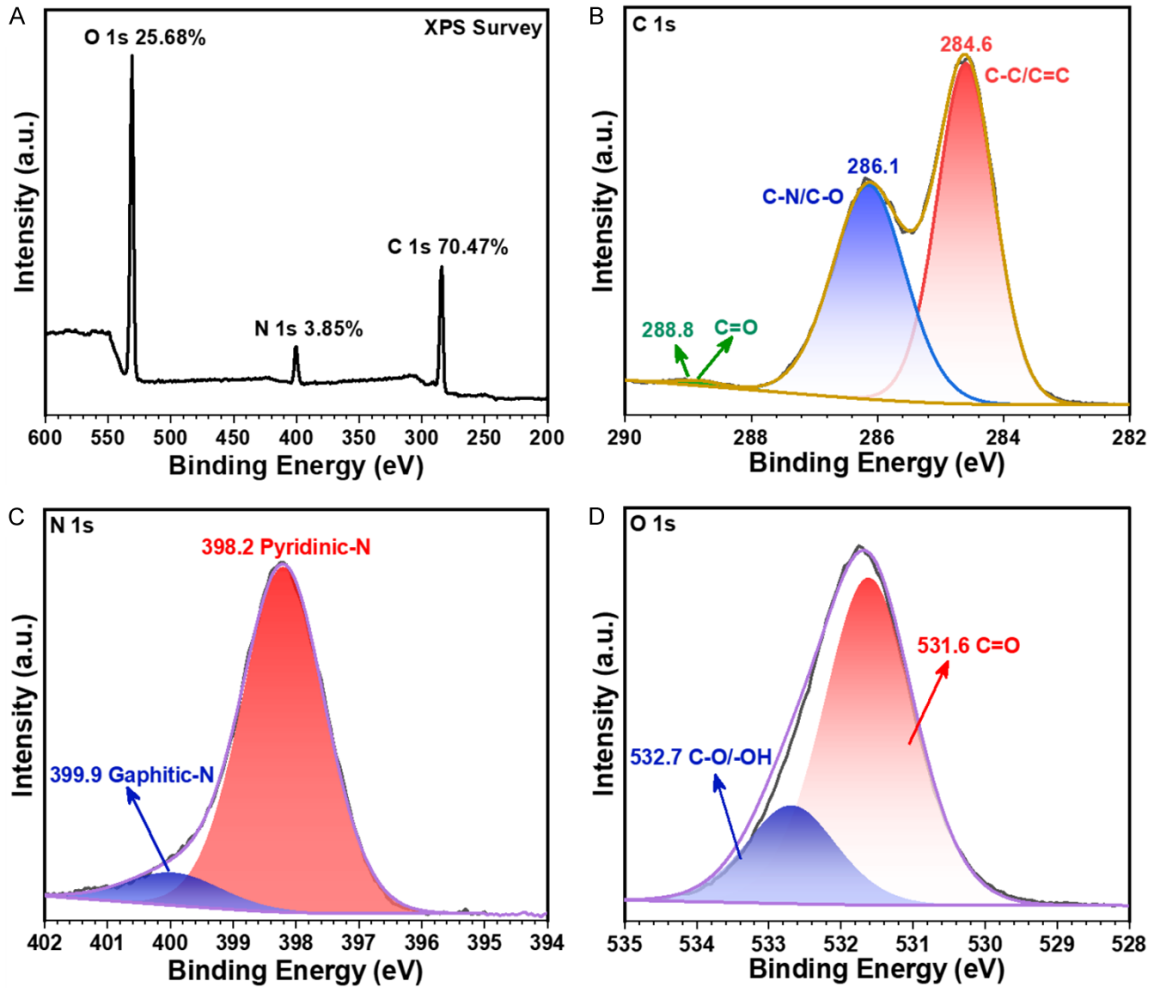

Figure 2. Composition of the N, CQ-dots. A. X-ray photoelectron spectroscopy (XPS) survey spectrum of the N, CQ-dots. B-D. High-resolution XPS C 1s, N 1s, and O 1s spectra of the N, CQ-dots.

for successful carbon quantum dots formation [21, 22].

Composition analysis

To further elucidate the chemical composition, the synthesized N, CQ-dots were systematically characterized via X-ray photoelectron spectrometer (XPS). The full-scan XPS spectrum (**Figure 2A**) demonstrates the presence of carbon (C), nitrogen (N), and oxygen (O) elements with atomic percentages of 70.47%, 3.85%, and 25.68%, respectively, confirming successful nitrogen doping in the carbon quantum dots. In addition, the elevated O content means abundant surface oxygen functionalities, which may enhance hydrophilicity and interfacial interactions. High-resolution XPS C 1s spectra (**Figure 2B**) resolve three distinct C species: sp^2/sp^3 hybridized C-C/C=C (284.6 eV), C-N/C-O (286.1 eV), and C=O (288.8 eV) [23]. Similarly, the N 1s spectrum (**Figure 2C**) exhibits two prominent peaks at 398.2 eV (pyridinic N) and 399.9 eV (graphitic N), indicating effective N incorporation into the C lattice [24]. Deconvolution of the O 1s band (**Figure 2D**) identifies two binding energy components at 531.6 eV (C=O) and 532.7 eV (C-O/C-O-H), corroborating the existence of carboxylic and hydroxyl groups on the surface [25].

Surface state of the N, CQ-dots

Fourier transform infrared (FTIR) spectrometer and nuclear magnetic resonance (NMR) spectroscopy were employed for surface functional group characterization of N, CQ-dots. Comparative analysis of the FTIR spectrum of

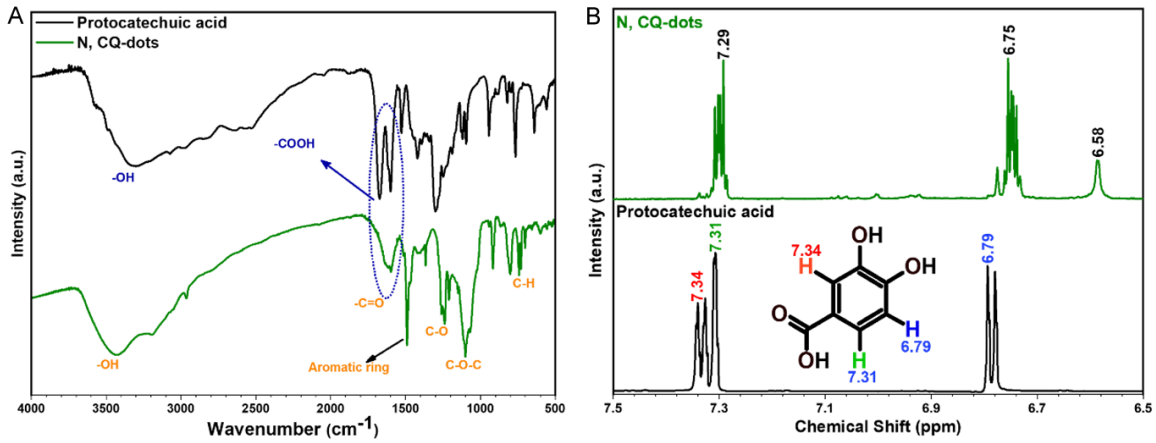

Figure 3. Surface groups of the N, CQ-dots. A. Fourier Transform Infrared (FTIR) spectra of the N, CQ-dots (green line), and protocatechuic acid (black line). B. Hydrogen nuclear magnetic resonance (^{1}H NMR) spectrum of the N, CQ-dots (green line), and protocatechuic acid (black line).

precursor (**Figure 3A**, black line), in the N, CQ-dots, the broad absorption band at 3431 cm^{-1} is attributed to the stretching vibration of -OH, and the sharp peak at 1638 cm^{-1} is assigned to the stretching vibration of -C=O (**Figure 3A**, green line), confirming the preservation of residual -COOH and -OH groups from the precursor post-pyrolysis [26]. Furthermore, the absorption band of 1489 cm^{-1} derived from the stretching vibration of the aromatic ring [27]. In addition, the prominent absorption at ~1100 cm^{-1} (C-O-C) indicates enhanced aqueous solubility [26]. The bond of 1260 cm^{-1} originates from the stretching vibration of C-O, the peaks at 801 and 742 cm^{-1} are separately ascribed to the stretching vibration and out-of-plane bending vibration of C-H on the aromatic ring [28, 29]. To better understand the structure of the N, CQ-dots, characteristic hydrogen nuclear magnetic resonance spectroscopy (^{1}H NMR) of precursor was recorded and treated as a standard reference. The results of ^{1}H NMR spectra are shown in **Figure 3B**. Protocatechuic acid features three kinds of chemical shifts located at 6.79, 7.31, and 7.34 ppm, and these chemical shifts are caused by hydrogen vibration of the benzene ring (black line). As shown in **Figure 3B** (green line), N, CQ-dots shows the almost same chemical shift at 6.75 and 7.29 ppm, which proves that the surface characteristic structure of the N, CQ-dots is highly consistent with that of precursors. In addition, aromatic hydrogen at 6.58 ppm is also observed on the surface of the N, CQ-dots, which may be caused by the introduction of the N element. In summary, combined with the results of FTIR, and ^{1}H NMR analysis, surface functional groups of the N, CQ-dots are dominated by residual -COOH and -OH groups of protocatechuic acid, and their distribution is highly consistent with that of the precursor, which indicates that the N, CQ-dots may retain the antimicrobial ability of the protocatechuic acid.

Optical properties of the N, CQ-dots

The optical properties of the N, CQ-dots were systematically investigated through UV-Vis and photoluminescence (PL) spectroscopy. The absorption spectrum exhibits two absorption maxima bands at 275 and 428 nm (**Figure 4A**, black line), attributed to π⟶π* transition of the aromatic C=C bond and n⟶π* transitions of the aromatic sp^2 system containing C=O and C=N bonds, respectively [26, 30]. In the PL spectrum of the N, CQ-dots (**Figure 4A**, red line), N, CQ-dots dispersed in aqueous solution exhibits the strongest emission center at 547 nm under the irradiation of a handheld UV lamp at 395 nm. In addition, the N, CQ-dots show excitation wavelength independent emissions properties (**Figure 4B**), indicating the stable energy level structure may promote the photodynamic antimicrobial ability of the N, CQ-dots.

Antibacterial testing of the N, CQ-dots

An effective method of sterilization is essential due to the potential risk of bacterial infection caused by bedsores. The observations led us to exert further research on the bactericidal

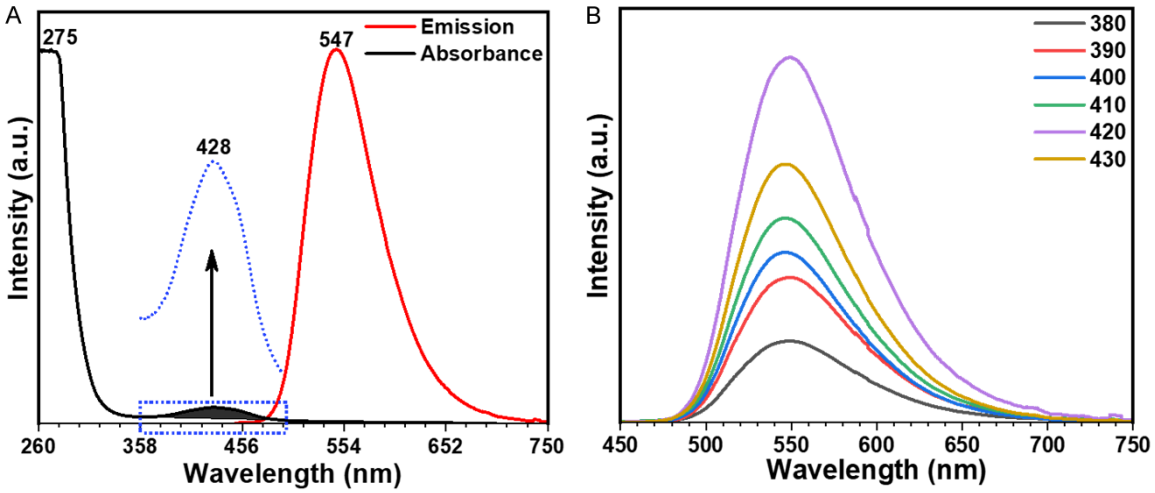

Figure 4. Optical properties of the N, CQ-dots. A. ultraviolet-to-visible (UV-vis) absorption (black line) and photoluminescence (PL) spectrum (red line) of the N, CQ-dots. B. PL spectrum of the N, CQ-dots excited by different wavelength.

properties of the N, CQ-dots, centered around their significant photodynamic effect *E. coli* and S. *aureus* were selected as typical strains of Gram-negative and Gram-positive bacteria, two clinically relevant pathogens. To elucidate the interaction dynamics between N, CQ-dots and microbial cells, colony-forming unit (CFU) assays were performed to quantify viable bacterial populations following varied irradiation durations and nanoparticle concentrations. Time-dependent assessments revealed a progressive enhancement in antimicrobial activity, with complete inhibition observed at extended exposure intervals (**Figure 5A**). Under 808 nm laser irradiation for 5 minutes, the bacterial load decreased proportionally with increasing N, CQ-dots concentration, as evidenced by reduced colony counts (**Figure 5B**, **5C**). A threshold concentration of 100 μg/mL was established as the minimum bactericidal concentration (MBC), effectively eradicating both E. coli and S. aureus within the experimental framework. Consequently, these findings corroborate the robust in vitro bactericidal efficacy of N, CQ-dots, positioning them as promising candidates for combating recalcitrant wound infections through non-antibiotic mechanisms.

SYTO9 is a cell-permeant fluorogenic nucleic acid stain that intercalates into double-stranded DNA, producing bright green fluorescence with excitation/emission maxima at 483/503 nm [31]. PI, in contrast, selectively penetrates compromised membranes of necrotic cells, binding to nucleic acids and emitting red fluorescence. To investigate membrane integrity disruption mechanisms, live/dead bacterial viability assays were performed. Confocal imaging (**Figure 6A**) reveals exclusive SYTO9 green fluorescence in the PBS control group under 808 nm irradiation, demonstrating intact bacterial membranes with minimal permeabilization. Conversely, N, CQ-dots combined with 808 nm irradiation elicit pronounced PI uptake, evidenced by intensified red fluorescence, indicating severe membrane damage through photodynamic oxidation. Scanning electron microscope (SEM) further corroborates these findings. Control bacteria in the PBS group maintain characteristic morphology with smooth cell surfaces for both E. coli and S. aureus. However, N, CQ-dots-mediated photodynamic treatment induces catastrophic structural alterations, including membrane blebbing, cytoplasmic leakage, and cellular fragmentation (**Figure 6B**). These morphological transformations align with ROS-induced lipid peroxidation and mechanical destabilization of Gram-negative/Gram-positive bacterial envelopes. Collectively, these data establish that the synergistic action of N, CQ-dots and NIR irradiation effectively compromises membrane integrity, leading to bacterial eradication through non-antibiotic photodynamic mechanisms.

Discussion

Bacterial infections remain a critical global public health challenge, exacerbated by the escalating antimicrobial resistance crisis driv-

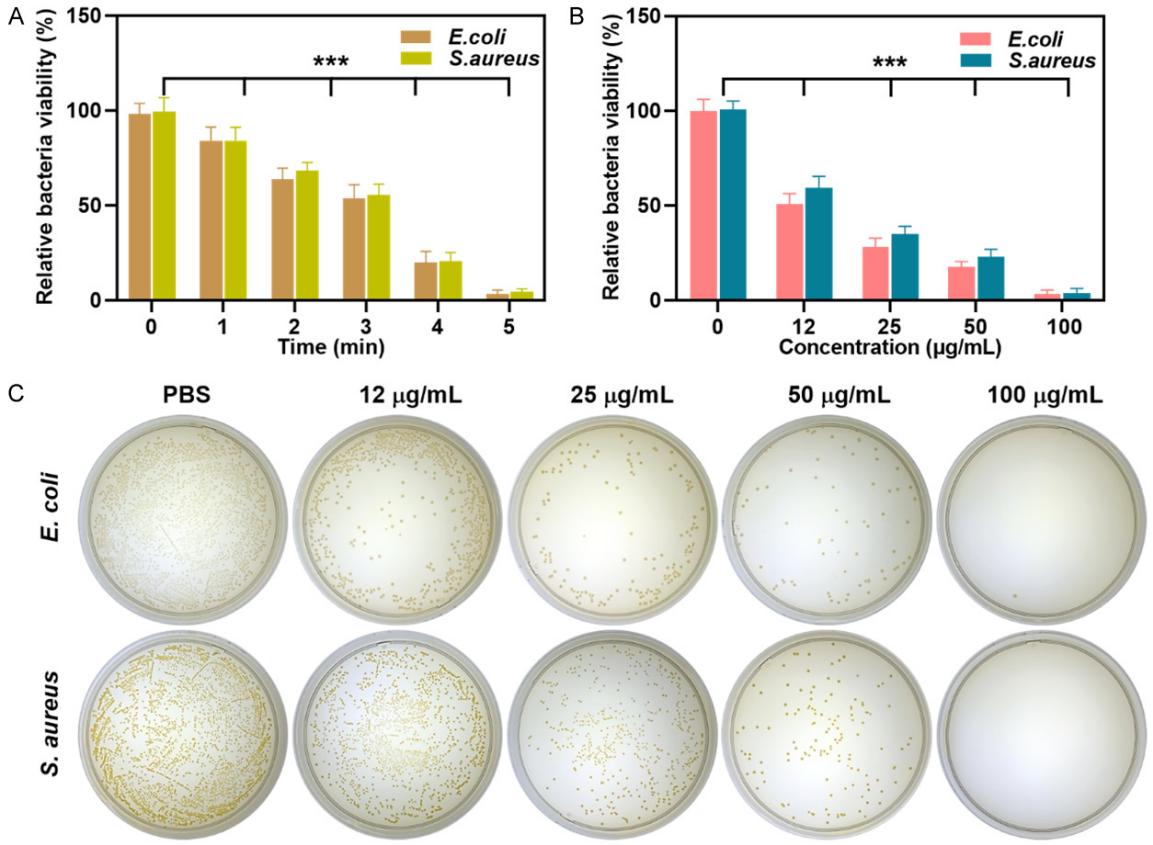

Figure 5. Antibacterial properties of the N, CQ-dots. A. The viability of *E. coli* and *S. aureus* is evaluated using the N, CQ-dots at different times. B. An analysis of the inhibition efficacy of the N, CQ-dots against *E. coli* and *S. aureus* at different concentrations. C. Images of *E. coli* and *S. aureus* colonies after treatment with the N, CQ-dots at 808 nm laser for five minutes at various concentrations.

en by antibiotic overuse. To address this, we have successfully converted antibiotics (protocatechuic acid) into N, CQ-dots by solvothermal method using N, N-dimethylformamide as solvent and N source. This strategy aligns with recent advances in nanomaterial-based antimicrobial therapies, offering a promising alternative to conventional antibiotics.

The synthesized N, CQ-dots exhibited a uniform particle size of ~3.5 nm, consistent with studies demonstrating that sub-5 nm CQ-dots achieve superior antibacterial efficacy due to enhanced cellular membrane penetration. Notably, our findings expand on Sun et al.'s work by demonstrating that solvothermal carbonization preserves key functional groups (*e.g.*, -OH, -COOH) from the precursor and may synergistically enhance bacterial targeting [32]. This retention of structural motifs, evidenced by FTIR and NMR analyses, suggests that the antimicrobial activity stems not only from physical interactions (e.g., membrane disruption) but also from chemical compatibility with bacterial cell walls, such as hydrogen bonding between carboxyl groups and peptidoglycan layers.

Generally, CQ-dots require light-induced generation of ROS to exert antimicrobial abilities. In contrast, their antibacterial activity is significantly diminished in the absence of photoexcitation. Ren et al. demonstrated that CQ-dots retain intrinsic carbonaceous domains during carbonization, enhancing dark-state antibacterial efficacy through ROS-independent mechanisms supported by structural stability [33]. Building on this, we conducted FTIR analysis to compare structural features of N, CQ-dots and protocatechuic acid. The spectra revealed nearly identical characteristic absorption peaks for both materials, including -OH, -COOH, and aromatic ring functionalities. Furthermore, N, CQ-dots exhibited a distinct ether bond vibration signal (1050 cm^{-1}), likely arising from

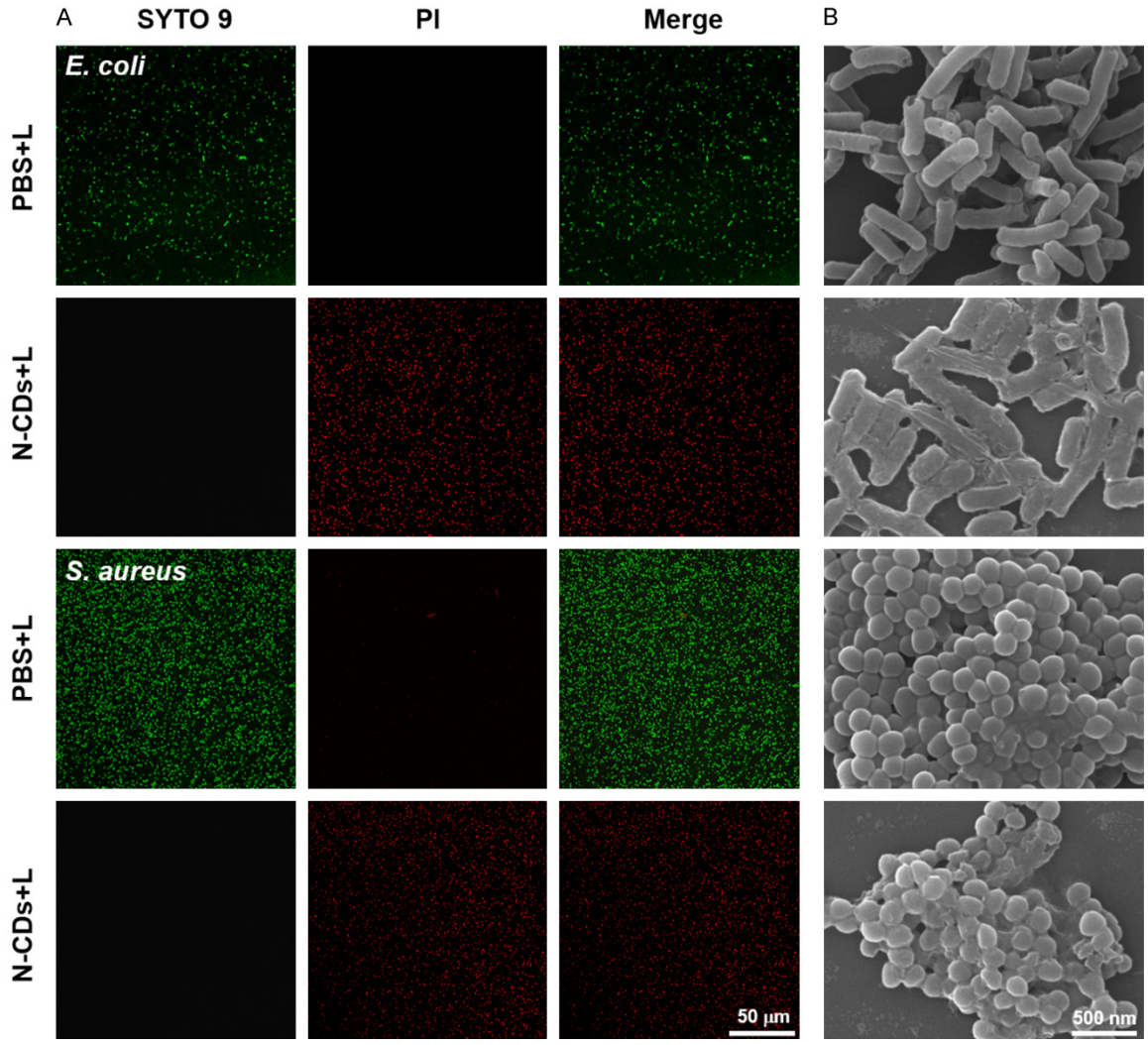

Figure 6. Antibacterial characterization of the N, CQ-dots. A. The live/dead staining of bacteria in control and experimental groups was visualized using laser confocal fluorescent images, scale bar 50 μm. B. A comparison of scanning electron microscope (SEM) images of *E. coli* and *S. aureus* in corresponding treatment groups, scale bar =500 nm. L: 808 nm laser.

oxygen participation during solvothermal synthesis and contributing to superior aqueous dispersion.

To further elucidate surface chemistry, proton resonance signals were analyzed via superconducting NMR spectroscopy. The chemical shifts of N, CQ-dots and protocatechuic acid in the 7.5-6.7 ppm range showed strong alignment, confirming preservation of aromatic structures from the precursor. Importantly, high-efficiency photodynamic therapy necessitates CQ-dots with broad light absorption capabilities [13]. While Shi et al. reported Sm-doped CQ-dots with absorption spanning 300-1100 nm, the N, CQ-dots synthesized here exhibited a narrower range (260-500 nm), highlighting a critical area for optimization through heteroatom doping or hybrid nanostructures [34]. Notably, antibacterial assays demonstrated ~100% efficacy under 808 nm excitation, indicating two-photon/multi-photon absorption properties. This feature positions N, CQ-dots as promising candidates for non-invasive photodynamic therapy, particularly for deep-tissue infections where near-infrared activation minimizes collateral damage.

Comparative analysis with existing literature reveals both congruent and contradictory findings. While Jou et al. reported CdSe/ZnS quantum dots [35] and Peng et al. reported CdTe

quantum dos [36] with broader light absorption, their synthesis involved toxic heavy metals, raising biosafety concerns. In contrast, our metal-free N, CQ-dots avoid cytotoxicity risks, aligning with recent trends toward eco-friendly nanomaterials. However, this work shares a limitation with most CQ-dot studies: the reliance on in vitro models. Future investigations should validate efficacy in animal models of bacterial infection to assess translational potential.

The clinical implications of this work are significant. First, the dual-mode antibacterial activity reduces dependence on external light sources, addressing practical challenges in wound care settings. Second, the two-photon absorption property enables NIR-triggered PDT, which is safer and more tissue-penetrating than UV or blue light commonly used in conventional PDT. These advantages position N, CQ-dots as candidates for next-generation antimicrobial agents, particularly for biofilm-associated infections resistant to conventional therapies. Despite these advancements, several challenges remain. The scalability of solvothermal synthesis needs optimization for industrial applications, and long-term environmental impacts of CQ-dots require thorough evaluation. Additionally, while our FTIR/NMR data suggest structural retention, direct evidence of precursor-to-product molecular transformations could strengthen mechanistic claims.

Collectively, this study advances the mechanistic understanding of structure-property relationships in carbon nanomaterials and provides a scalable framework for developing sustainable antimicrobial agents. By integrating chemical intuition with materials science, we demonstrate how rational design of CQ-dots can address critical gaps in antimicrobial resistance management, offering a blueprint for future innovations in this field.

Conclusion

This study demonstrates the successful transformation of a natural antimicrobial agent into N, CQ-dots through a solvothermal protocol. Leveraging their intrinsic optoelectronic properties, these nanomaterials exhibit enhanced photodynamic inactivation efficacy, achieving >99.9% viability reduction against multidrug-resistant pathogens under 808 nm laser excitation. Mechanistic investigations reveal efficient cellular uptake by both Gram-negative *E. coli* and Gram-positive *S. aureus*, followed by ROS-mediated membrane disruption and intracellular content leakage. This platform presents a novel prophylactic strategy for pressure ulcer management, potentially preventing progression to systemic infections through localized antimicrobial action. Preclinical validation through in vivo models is warranted to establish their therapeutic translatability in biomedical applications. The present findings establish a paradigm for combating antimicrobial resistance while offering biocompatible nanomaterials with clinical translation potential.

Disclosure of conflict of interest

None.

Address correspondence to: Jia Sun, Department of Rehabilitation Medicine, Zhejiang Hospital, No. 12 Lingyin Road, Hangzhou 310000, Zhejiang, P. R. China. E-mail: s18895365161@outlook.com

References

[1] Smith DM, Snow DE, Rees E, Zischkau AM, Hanson JD, Wolcott RD, Sun Y, White J, Kumar S and Dowd SE. Evaluation of the bacterial diversity of pressure ulcers using bTEFAP pyrosequencing. BMC Med Genomics 2010; 3: 41.

[2] Choo J, Nixon J, Nelson A and McGinnis E. Autolytic debridement for pressure ulcers. Cochrane Database Syst Rev 2019; 6: CD011331.

[3] Chen X, Huang B, Xiao H, An L, Su W and Yu D. Application of the Jigsaw puzzle flap based on freestyle perforators to repair large and deep ulcers on the buttocks. Front Surg 2022; 9: 739250.

[4] Hekmatpou D, Ahmadian F, Eghbali M and Farsaei S. Henna (Lawsonia inermis) as an inexpensive method to prevent decubitus ulcers in critical care units: a randomized clinical trial. J Evid Based Integr Med 2018; 23: 2515690X18772807.

[5] Searns JB. Delaying antimicrobials for pediatric bone and joint infections: balancing clinical risks with diagnostic benefits. Front Pediatr 2022; 10: 975221.

[6] Darden DB, Kelly LS, Fenner BP, Moldawer LL, Mohr AM and Efron PA. Dysregulated immunity and immunotherapy after sepsis. J Clin Med 2021; 10: 8.

[7] Li Y, Tan Z, Cheng Y, Zhang J and Wu H. High-viscosity versus low-viscosity cement for the treatment of vertebral compression fractures:

a meta-analysis of randomized controlled trials. Medicine (Baltimore) 2022; 101: e31544.
[8] Park MO and Lee SH. Effects of seating education and cushion management for adaptive sitting posture in spinal cord injury: two case reports. Medicine (Baltimore) 2019; 98: e14231.
[9] Yang J, Xiao C, Wen H, Sun K, Wu X and Feng X. Effect evaluation of platelet-rich plasma combined with vacuum sealing drainage on serum inflammatory factors in patients with pressure ulcer by intelligent algorithm-based CT image. Comput Math Methods Med 2022; 2022: 8916076.
[10] Sundvall PD, Elm M, Gunnarsson R, Mölstad S, Rodhe N, Jonsson L and Ulleryd P. Antimicrobial resistance in urinary pathogens among Swedish nursing home residents remains low: a cross-sectional study comparing antimicrobial resistance from 2003 to 2012. BMC Geriatr 2014; 14: 30.
[11] McGee WT, Nathanson BH, Lederman E and Higgins TL. Decubitus ulcers are associated with prolonged length of stay in critically ill patients. Crit Care 2013; 17: P465.
[12] Han Y, Liccardo L, Moretti E, Zhao H and Vomiero A. Synthesis, optical properties and applications of red/near-infrared carbon dots. J Mater Chem 2022; 10: 11827-11847.
[13] Li P, Sun L, Xue S, Qu D, An L, Wang X and Sun Z. Recent advances of carbon dots as new antimicrobial agents. SmartMat 2022; 3: 226-248.
[14] Huang S, Song Y, Zhang JR, Chen X and Zhu JJ. Antibacterial carbon dots-based composites. Small 2023; 19: e2207385.
[15] Wang B and Lu S. The light of carbon dots: from mechanism to applications. Matter 2022; 5: 110-149.
[16] Yu Y, Zeng Q, Tao S, Xia C, Liu C, Liu P and Yang B. Carbon dots based photoinduced reactions: advances and perspective. Adv Sci 2023; 10: e2207621.
[17] De BS, Wasewar KL, Dhongde VR, Ingle AA and Mondal H. Experimental and modeling of reactive separation of protocatechuic acid. Chem Eng Res and Des 2018; 132: 593-605.
[18] Deuchande T, Fundo JF, Pintado ME and Amaro AL. Protocatechuic acid as an inhibitor of lipid oxidation in meat. Meat Sci 2024; 213: 109519.
[19] Gutierrez-Zetina SM, Gonzalez-Manzano S, Perez-Alonso JJ, Gonzalez-Paramas AM and Santos-Buelga C. Preparation and characterization of protocatechuic acid sulfates. Molecules 2019; 24: 307.
[20] Meng X, Song Y, Jing Q and Zhao H. Self-precipitation of highly purified red emitting carbon dots as red phosphors. J Phys Chem Lett 2023; 14: 9176-9182.
[21] Meng X, Wang M, Lin J, Wang L, Liu J, Song Y, Jing Q and Zhao H. Intermediate aminophenol enables hectogram-scale synthesis of highly bright red carbon quantum dots under ambient conditions. Chem Sci 2024; 15: 9806-9813.
[22] Xu W, Han Q, Ji C, Zeng F, Zhang X, Deng J, Shi C and Peng Z. Solid-state, hectogram-scale preparation of red carbon dots as phosphor for energy-transfer-induced high-quality white LEDs with CRI of 97. Small 2023; 19: e2304123.
[23] Wang B, Wei Z, Sui L, Yu J, Zhang B, Wang X, Feng S, Song H, Yong X, Tian Y, Yang B and Lu S. Electron-phonon coupling-assisted universal red luminescence of o-phenylenediamine-based carbon dots. Light Sci Appl 2022; 11: 172.
[24] Zhang Q, Wang F, Wang R, Liu J, Ma Y, Qin X and Zhong X. Activating one/two-photon excited red fluorescence on carbon dots: emerging n→πphoton transition induced by amino protonation. Adv Sci 2023; 10: e2207566.
[25] Ding H, Wei JS, Zhang P, Zhou ZY, Gao QY and Xiong HM. Solvent-controlled synthesis of highly luminescent carbon dots with a wide color gamut and narrowed emission peak widths. Small 2018; 14: e1800612.
[26] Liu J, Kong T and Xiong HM. Mulberry-leaves-derived red-emissive carbon dots for feeding silkworms to produce brightly fluorescent silk. Adv Mater 2022; 34: e2200152.
[27] Zhang Q, Wang R, Feng B, Zhong X and Ostrikov K. Photoluminescence mechanism of carbon dots: triggering high-color-purity red fluorescence emission through edge amino protonation. Nat Commun 2021; 12: 6856.
[28] Jiao Y, Liu Y, Meng Y, Gao Y, Lu W, Liu Y, Gong X, Shuang S and Dong C. Novel processing for color-tunable luminescence carbon dots and their advantages in biological systems. ACS Sustain Chem Eng 2020; 8: 8585-8592.
[29] Li P, Xue S, Sun L, Zong X, An L, Qu D, Wang X and Sun Z. Formation and fluorescent mechanism of red emissive carbon dots from o-phenylenediamine and catechol system. Light Sci Appl 2022; 11: 298.
[30] Chen R, Wang Z, Pang T, Teng Q, Li C, Jiang N, Zheng S, Zhang R, Zheng Y, Chen D and Yuan F. Ultra-narrow-bandwidth deep-red electroluminescence based on green plant-derived carbon dots. Adv Mater 2023; 35: e2302275.
[31] Zhang Z, Xu Y, Zhu T, Sang Z, Guo X, Sun Y, Hao Y and Wang W. Hypoxia mitigation by manganese-doped carbon dots for synergistic photodynamic therapy of oral squamous cell carcinoma. Front Bioeng Biotechnol 2023; 11: 1153196.

[32] Sun B, Wu F, Zhang Q, Chu X, Wang Z, Huang X, Li J, Yao C, Zhou N and Shen J. Insight into the effect of particle size distribution differences on the antibacterial activity of carbon dots. J Colloid Interface Sci 2021; 584: 505-519.
[33] Wu Y, Li C, van der Mei HC, Busscher HJ and Ren Y. Carbon quantum dots derived from different carbon sources for antibacterial applications. Antibiotics 2021; 10: 623.
[34] Shi H, Yin Y, Xu H, Qu X, Wang H and An Z. Samarium doped carbon dots for near-infrared photo-therapy. Chem Eng J 2024; 488: 150661.
[35] Jou AF, Lu CH, Ou YC, Wang SS, Hsu SL, Willner I and Ho JA. Diagnosing the miR-141 prostate cancer biomarker using nucleic acid-functionalized CdSe/ZnS QDs and telomerase. Chem Sci 2015; 6: 659-665.
[36] Peng C, Zhang Y, Qian Z and Xie Z. Fluorescence sensor based on glutathione capped CdTe QDs for detection of Cr^{3+} ions in vitamins. Food Sci Hum Wellness 2018; 7: 71-76.